

Modeling Quasar UV/Optical Variability with the Corona-heated Accretion-disk Reprocessing (CHAR) Model

Mouyuan Sun¹, Yongquan Xue^{2,3}, Hengxiao Guo^{4,5,6}, Junxian Wang^{2,3}, W. N. Brandt^{7,8,9}, Jonathan R. Trump¹⁰, Zhicheng He^{2,3}, Tong Liu¹, Jianfeng Wu¹, and Haikun Li¹ Department of Astronomy, Xiamen University, Xiamen, Fujian 361005, People's Republic of China; msun88@xmu.edu.cn

Department of Astronomy, Xiamen University, Xiamen, Fujian 361005, People's Republic of China; msun88@xmu.edu.cn

CAS Key Laboratory for Research in Galaxies and Cosmology, Department of Astronomy, University of Science and Technology of China, Hefei 230026, People's Republic of China

School of Astronomy and Space Science, University of Science and Technology of China, Hefei 230026, People's Republic of China
 ⁴ Department of Astronomy, University of Illinois at Urbana-Champaign, Urbana, IL 61801, USA
 ⁵ National Center for Supercomputing Applications, University of Illinois at Urbana-Champaign, Urbana, IL 61801, USA
 ⁶ Department of Physics and Astronomy, 4129 Frederick Reines Hall, University of California, Irvine, CA 92697-4575, USA
 ⁷ Department of Astronomy & Astrophysics, 525 Davey Lab, The Pennsylvania State University, University Park, PA 16802, USA
 ⁸ Institute for Gravitation and the Cosmos, 525 Davey Lab, The Pennsylvania State University, University Park, PA 16802, USA
 ⁹ Department of Physics, 104 Davey Lab, The Pennsylvania State University, University Park, PA 16802, USA
 ¹⁰ Department of Physics, University of Connecticut, Storrs, CT 06269, USA

Received 2020 July 14; revised 2020 August 18; accepted 2020 August 22; published 2020 October 7

Abstract

The rest-frame UV/optical variability of the quasars in the Sloan Digital Sky Survey Stripe 82 is used to test the Corona-Heated Accretion-disk Reprocessing (CHAR) model of Sun et al. We adopt our CHAR model and the observed black hole masses ($M_{\rm BH}$) and luminosities (L) to generate mock light curves that share the same measurement noise and sampling as the real observations. Without any fine-tuning, our CHAR model can satisfactorily reproduce the observed ensemble structure functions for different $M_{\rm BH}$, L, and rest-frame wavelengths. Our analyses reveal that a luminosity-dependent bolometric correction is disfavored over the constant bolometric correction for UV/optical luminosities. Our work demonstrates the possibility of extracting quasar properties (e.g., the bolometric correction or the dimensionless viscosity parameter) by comparing the physical CHAR model with quasar light curves.

Unified Astronomy Thesaurus concepts: Accretion (14); Active galactic nuclei (16); Quasars (1319); Supermassive black holes (1663)

Supporting material: figure set

1. Introduction

Active galactic nucleus (AGN) UV/optical variability offers a new way to resolve the broad emission-line regions (Blandford & McKee 1982) as well as the accretion disks (Collin-Souffrin 1991; Krolik et al. 1991) and probe the density of the outflowing gas density (He et al. 2019; Li et al. 2019). AGN UV/optical variability is most likely to be driven by time-dependent evolution of the central engine (i.e., accretion disk) because many studies (Kelly et al. 2009; MacLeod et al. 2010; Sun et al. 2015; Caplar et al. 2017) found that AGN UV/optical variability depends at least on black hole mass $(M_{\rm BH})$ and luminosity (L). However, our physical understanding of AGN UV/optical variability is far from clear (Lawrence 2018). In a previous work (Sun et al. 2020), we proposed a Corona-Heated Accretion-disk Reprocessing (CHAR) model to explain the UV/optical variability of quasars. 11 In the CHAR model, the X-ray corona and the underlying cold accretion disk are magnetically coupled. Coronal magnetic fluctuations can induce coherent fluctuations in the disk heating rate which alter the disk temperature and UV/optical luminosity. We demonstrated that the CHAR model can explain high-quality Kepler AGN light curves, as well as the larger-than-expected interband time lags and the multiwavelength structure functions (i.e., the variability

amplitude as a function of timescale; see also Section 2) of NGC 5548. We also showed that the CHAR model has the potential to explain the dependence of AGN UV/optical variability parameters upon $M_{\rm BH}$, L, and rest-frame wavelength (λ_{rest}) . In Sun et al. (2020), we additionally suggested that the CHAR model could be used to fit the observed UV/optical variability of quasars and laid out a plan for future work that would make a more detailed comparison between the CHAR model predictions and the observational results of the correlations between quasar UV/optical variability and physical properties. The Sloan Digital Sky Survey (SDSS; Gunn et al. 2006) Stripe 82 (hereafter SDSS S82) quasar observations provide a valuable data set for fitting by our physical CHAR model. Compared with adopting empirical stochastic models (e.g., the popular CAR(1) model, a.k.a., the damped random walk model) to fit AGN light curves (e.g., Kelly et al. 2009; MacLeod et al. 2010), our modeling results have straightforward physical implications.

This paper is formatted as follows. In Section 2, we introduce the SDSS S82 quasar light curves and the corresponding ensemble structure functions. In Section 3, we present our mock ensemble structure functions and compare them with the observed ones. In Section 4, we discuss our results and present a recipe to simulate quasar multiband stochastic light curves. Our conclusions are summarized in Section 5.1. The Schwarzschild radius is $R_{\rm S} \equiv 2GM_{\rm BH}/c^2$, where G and c are the gravitational constant and speed of light, respectively.

¹¹ We use the term quasars to generically refer to AGNs with optical broad emission lines, regardless of luminosity. That is, AGNs and quasars are used interchangeably in this work.

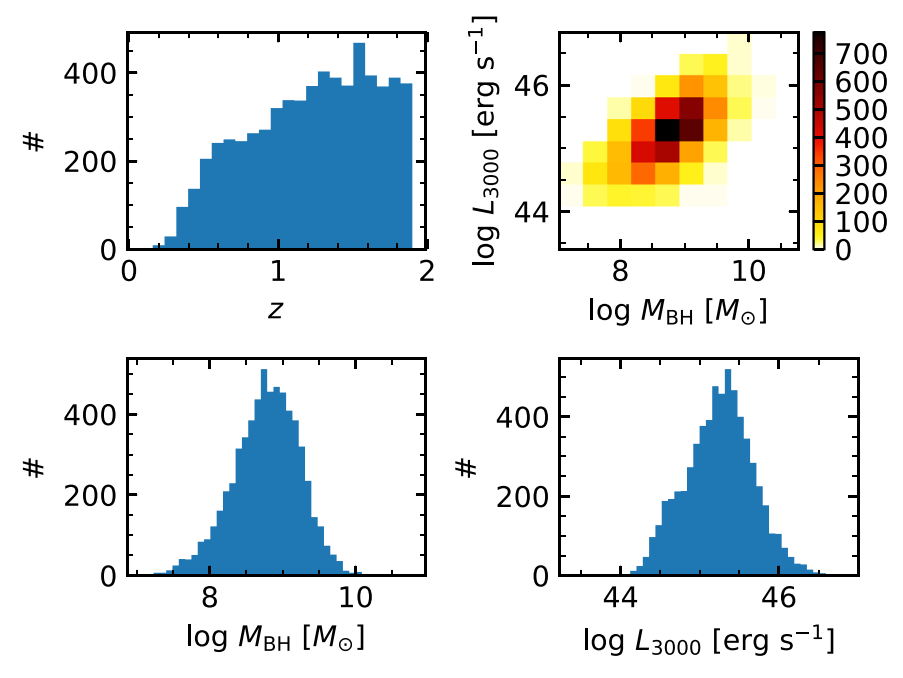


Figure 1. Distributions of redshift, $M_{\rm BH}$, and $L_{\rm bol}$ for the parent sample of the SDSS S82 quasars. Most sources have z>1 (the upper-left panel) and span more than 2 dex in $M_{\rm BH}$ and $L_{\rm bol}$.

2. Sample Construction and Observed Variability

Following MacLeod et al. (2010), we consider the variability data of SDSS S82 quasars with multiepoch (on average > 60 epochs) and multiband (i.e., ugriz; see Fukugita et al. 1996) observations. The light curves 2 are well calibrated by Ivezić et al. (2007) and Sesar et al. (2007). First, we cross-match these quasars with the catalog of SDSS DR7 quasar properties (Shen et al. 2011) and obtain their redshifts (z), $M_{\rm BH}$, and the restframe $\lambda = 3000 \,\text{Å}$ luminosity (i.e., $L_{3000} = \lambda \, L_{\lambda}$ for the restframe $\lambda = 3000 \,\text{Å}$). Second, we only select sources with either H β or Mg II virial black hole mass estimates (i.e., z < 1.9); we do not adopt the C IV black hole mass estimator, as C IV often shows (nonvirial) outflow signatures (e.g., Richards et al. 2011; Denney 2012; Sun et al. 2018a), and the scatter of the ratio of the C IV-based $M_{\rm BH}$ to the H β -based one is substantial (≲1 dex) unless detailed empirical corrections are applied (e.g., Coatman et al. 2017; Marziani et al. 2019; Zuo et al. 2020). Radio-loud (i.e., radio-loudness $R \equiv L_{\nu}(6 \text{ cm})/L_{\nu}(2500 \text{ Å})$ being greater than 10) sources are removed. We reject light curves with less than 40 epochs. ¹³ The resulting parent sample consists of 6271 SDSS S82 quasars, and will be used for subsequent variability modeling. The distributions of redshift, $M_{\rm BH}$, and L_{3000} for the parent sample are shown in Figure 1.

Previous studies (Kelly et al. 2009; MacLeod et al. 2010; Sun et al. 2015, 2018b; Caplar et al. 2017) show that quasar UV/optical variability depends at least on $M_{\rm BH}$, L, and restframe wavelength ($\lambda_{\rm rest}$). The wavelengths at which the ugriz filters are the most sensitive are 3543 Å (u band), 4770 Å (g band), 6231 Å (r band), 7625 Å (i band), and 9134 Å (z band), respectively. ¹⁴ For a given band, the corresponding

rest-frame wavelengths of observed AGNs depend on redshifts. We construct four rest-frame wavelength cases by following the redshift criteria in Figure 3; for each case, these narrow redshift ranges are chosen to ensure that the corresponding rest-frame wavelengths for different SDSS filters are similar and to avoid strong broad emission-line coverage (note that the broad emission lines are likely to be less variable than their nearby continua; see, e.g., MacLeod et al. 2012; Sun et al. 2015). Let us take the 1900 Å case (i.e., the shortest $\lambda_{\rm rest} \simeq 4770/(1+1.5) = 1908 \,\text{Å}$ case) as an example. To obtain the shortest λ_{rest} light curves, we consider the u- and g-band observations of high-z quasars. The u band is sensitive to photons with 3000 Å $< \lambda_{\rm obs} < 4000$ Å. Therefore, we should avoid using u-band light curves for redshifts higher than 0.9; otherwise, the contamination of the prominent emission line, C IV or Ly α , cannot be eliminated (see the left panel of Figure 2). To ensure that g-band light curves probe the same λ_{rest} as the *u*-band ones, we should also avoid using the g-band light curves of z > 1.56 sources (see the right panel of Figure 2). We select the *u*-band light curves of 0.820 < z < 0.894 quasars and the g-band light curves of 1.450 < z < 1.550 quasars to probe the shortest $\lambda_{\rm rest} =$ 1908 Å (i.e., the 1900 Å case) continuum variability. At these redshift ranges, C III] is covered by u and g bands; however, C III] is relatively weak, with an equivalent width of $\sim 20 \,\text{Å}$ (Vanden Berk et al. 2001) and should have small contribution to the broadband fluxes. Other λ_{rest} -controlled subsamples (i.e., the 2400, 3180, and 4150 Å cases) are constructed following the same methodology (see Figure 3).

Each of the four $\lambda_{\rm rest}$ -matched subsamples (i.e., the 1900, 2400, 3180, and 4150 Å cases) is divided into five "shells" according to $M_{\rm BH}$, and each shell has a $\log M_{\rm BH}$ width of 0.5 dex (i.e., the typical 1σ uncertainty of the virial $M_{\rm BH}$ estimators; for a review, see Shen 2013), starting from $\log M_{\rm BH} = 7.5$ (see the lower-left panel of Figure 1). Each $M_{\rm BH}$ shell is further split into several L_{3000} bins following the methodology in Figure 3. Note that only L_{3000} bins with more

¹² These data can be downloaded from http://faculty.washington.edu/ivezic/macleod/qso_dr7/Southern.html.

 $^{^{13}}$ Only a small number of SDSS S82 light curves have less than 40 observations (see Figure 2 of MacLeod et al. 2010).

¹⁴ Please refer to http://skyserver.sdss.org/dr1/en/proj/advanced/color/sdssfilters.asp.

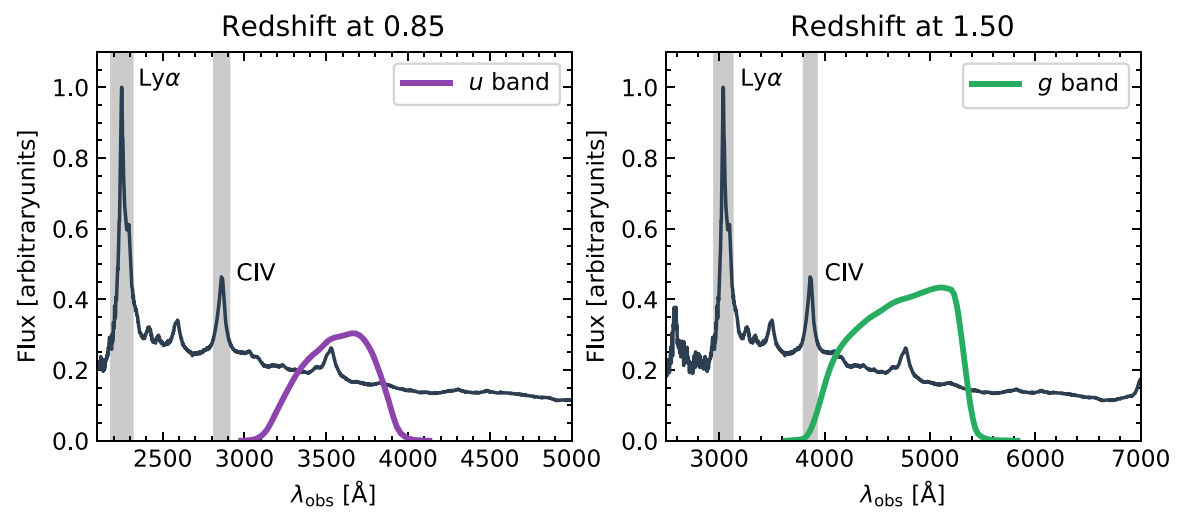


Figure 2. Illustration of redshift bins for defining the rest-frame continuum wavelengths. Left: the Vanden Berk et al. (2001) composite SDSS spectrum is shown with the SDSS u-band filter response curve for a quasar at z = 0.85. Right: the same as the left panel, but for a quasar at z = 1.50 and the SDSS g band. If one considers higher-redshift u- or g-band light curves, the contamination of strong broad emission lines (e.g., C IV, Ly\alpha; i.e., the shaded regions) is significant.

than 20 sources will be considered in subsequent analyses. For each bin, we calculate the corresponding median $\log M_{\rm BH}$ and $\log L_{3000}$. We then assume that all quasars in a bin have the same black hole mass and bolometric luminosity (i.e., the median values), as the bolometric corrections (see Section 3) and virial $M_{\rm BH}$ estimators are only valid in a sample-averaged

For each bin, we use the quasar light curves to calculate the ensemble structure function following the methodology of MacLeod et al. (2012) and Sun et al. (2015). That is, the statistical dispersion of two magnitude measurements (Δm) as a function of the corresponding rest-frame ¹⁵ time interval (Δt) is calculated as

$$SF = 0.74IQR(\Delta m), \tag{1}$$

where IQR(Δm) is the 25%–75% interquartile range of Δm ; the constant 0.74 normalizes the IQR to be equivalent to the standard deviation of a Gaussian distribution.

For some sources, the light curves have a few outlier data points, i.e., a sudden increment of more than 1 magnitude. To properly reject such outliers, we perform the following analysis. First, we use the CAR(1) model to fit each light curve. The CAR(1) model has been widely used to fit quasar UV/optical light curves 16 (e.g., Kelly et al. 2009; MacLeod et al. 2010) although its validity on very short or long timescales has been questioned by several previous works (e.g., Mushotzky et al. 2011; Caplar et al. 2017; Guo et al. 2017; Smith et al. 2018). The CAR(1) model has the following covariance matrix

$$C_{i,j} = \frac{1}{2}\hat{\sigma}^2 \tau \exp(-\Delta t_{i,j}/\tau), \qquad (2)$$

where $\hat{\sigma}$ and τ are the variability amplitude (i.e., standard deviation) of two observations (i and j) on the timescale $\Delta t_{i,j} \equiv |t_i - t_j| = 1$ day and the damping timescale in units of days, respectively. Second, we use a modified version of the Python module qso fit.py¹⁷ of Butler & Bloom (2011) to calculate the likelihood of a light curve given the CAR(1) model (see Equation (2) in Butler & Bloom 2011), and we find the combination of $\hat{\sigma}$ and τ that maximizes the likelihood. ¹⁸ Third, we use the best-fitting $\hat{\sigma}$ and τ to obtain the expected mean light curve and its statistical dispersion following Butler & Bloom (2011). Fourth, we calculate the ratios of the absolute deviations between the observed and expected model light curves to the statistical dispersion for every epoch (hereafter the differential ratios). Fifth, we find the maximum value of the differential ratios; if the maximum differential ratio is larger than 3, the corresponding epoch is rejected. The resulting light curve is then refitted with the CAR(1) model. We iterate this procedure until the maximum differential ratio is smaller than 3. We stress that this process should not remove real (possibly non-CAR(1)) variability but only reject a few suspicious magnitude measurements. This is because the SDSS S82 quasar light curves are too sparse to distinguish between the CAR(1) model and other more complex stochastic processes (Sun et al. 2018b). These rejected data points often show unexpected strong flux variability (~0.3 mag) within a few days or sharp flux changes (\sim 1 mag) on timescales of months. For more than 60% of sources, no data point is rejected; for \sim 25% of sources, only one data point is rejected; for \sim 10% of sources, two data points are rejected; only for \$5\% of sources, more than two data points (but less than six) are rejected. Therefore, this procedure should have negligible effect on our results.

We can now use the light curves to obtain the corresponding ensemble structure functions. For a heterogeneous data sample, e.g., the quasar light-curve data from the Palomar Transient Factory, Caplar et al. (2017) point out that the observational

¹⁵ Throughout this work, the wavelengths and timescales of quasar features are always rest frame, unless otherwise specified.

16 Note that data points with measurement errors > 0.1 mag are ignored.

¹⁷ This module can be accessed from http://astro.berkeley.edu/~nat/qso_

selection.

18 We use the *scipy* global optimization function, *differential_evolution*, to find ..., ...,

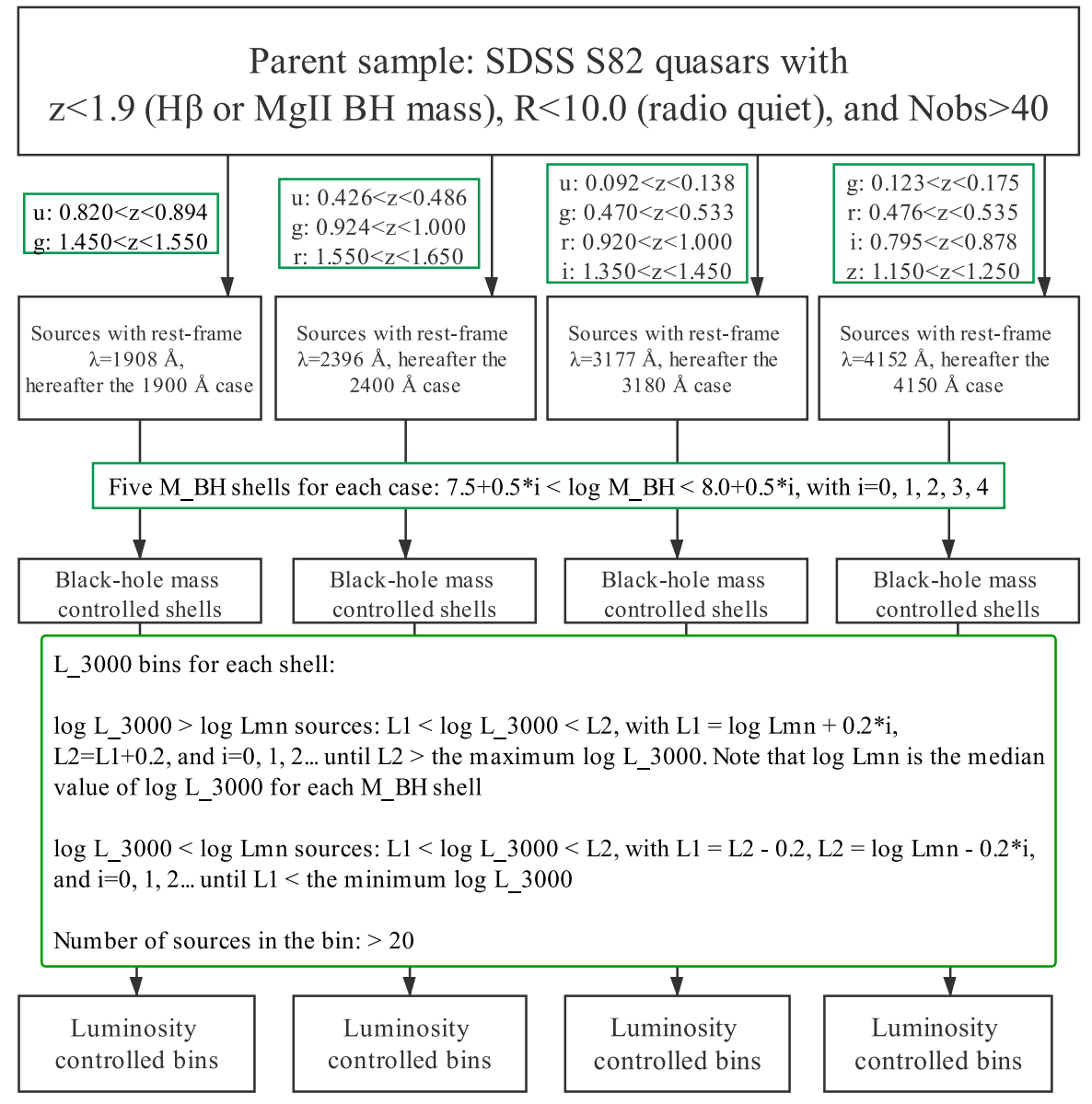


Figure 3. Our sample construction procedures to create λ_{rest} , M_{BH} , and L_{bol} controlled bins.

data pairs at some specific Δt might be dominated by a minor fraction of high-cadence sources; therefore, the resulting ensemble structure functions can be substantially biased. However, this bias should be not important in our case, as the light-curve samplings of SDSS S82 are quite uniform. Therefore, we simply use all data pairs for a given Δt to calculate the corresponding ensemble structure function. Note that the same strategy is adopted when calculating the model ensemble structure functions (see Section 3) for the sake of consistency. The resulting ensemble structure functions for the 1900 Å, 2400 Å, 3180 Å, and 4150 Å cases are shown in Figures 5–8, respectively. We do not plot the uncertainties of the ensemble structure functions; the uncertainties will be assigned to the model results because we will consider the real sampling and measurement errors when generating mock light curves (see Section 3). Note that the model-based error bars are consistent with the ones obtained from bootstrapping (with replacement) of quasars (i.e., similar to the procedure in Caplar et al. 2017).

3. Modeling SDSS S82 Quasar Multiband Variability

3.1. Model I: A Constant Bolometric Correction

We use our CHAR model to simulate quasar UV/optical light curves. This model assumes that the corona and the underlying cold thin disk are magnetically coupled; coronal magnetic fluctuations can induce variations of the disk heating rate. The resulting disk effective temperature is calculated by considering the vertically integrated thermal-energy conservation law (for more details, refer to Section 2 of Sun et al. 2020). The free parameters of the CHAR model are black hole mass, absolute accretion rate (\dot{M}), the dimensionless viscosity parameter α , and the variability amplitude of the heating rate ($\delta_{\rm mc}$).

For each bin, we use $\dot{M} = L_{\rm bol}/(\eta c^2)$ with the radiative efficiency $\eta = 0.1$ to estimate \dot{M} , where $L_{\rm bol} = 5$. $15L_{3000}$

 $[\]overline{}^{19}$ We do not use $\overline{L_{3000}}$ and the thin-disk theory to infer \dot{M} , because the inclination angle and the intrinsic extinction are unknown. Therefore, we prefer to adopt the empirical bolometric corrections to estimate \dot{M} .

(Richards et al. 2006); then, the model $M_{\rm BH}$ and \dot{M} are both fixed to be the observed ones. The remaining free parameters are α and $\delta_{\rm mc}$. We use the lowest $L_{\rm bol}$ bin of the 2400 Å case²⁰ to determine α and $\delta_{\rm mc}$. That is, we consider the combinations of α and $\delta_{\rm mc}$ by stepping through 14 values of $\delta_{\rm mc}$ from 0.1 to 0.7 in equal linear increments and 20 values of α from 10^{-2} to $10^{-0.2}$ in equal logarithmic increments. For each source in the bin, we use the same $M_{\rm BH}$, \dot{M} , $\delta_{\rm mc}$, and α as the CHAR model parameters to simulate the same number of mock light curves; the mock light curves are shifted to the observed frame according to their redshifts; the sampling patterns of the mock light curves are the same as the observed ones. We then add measurement noise to each mock light curve using uncorrelated white noise whose variance is the same as the observed one which is estimated from the observed ensemble structure functions at small Δt (i.e., $\Delta t < 4$ days). Subsequently, we calculate the mock ensemble structure function by using the mock light curves. We repeat the simulation 50 times. The differences between the mean results of the 50 mock ensemble structure functions and the observed ones for all combinations of α and $\delta_{\rm mc}$ are calculated. The best-fitting combination of α and $\delta_{\rm mc}$ (hereafter, α (best) and $\delta_{\rm mc}$ (best)) is the one that minimizes the differences between the observed and the model ensemble structure functions. We find that α (best) = 0.5 and $\delta_{\rm mc}$ (best) = 0.5 (i.e., the structure function of the natural logarithmic heating rate fluctuation on the timescale of 100 days is 0.5).

To model the ensemble structure functions of the rest of the bins, we fix α and $\delta_{\rm mc}$ to be α (best) and $\delta_{\rm mc}$ (best) determined above, respectively. We only change $\log M_{\rm BH}$ and $\log L_{\rm bol}$ according to the observed values, i.e., there is no free parameter in the following modeling procedures. For the rest of the bins of each case, we generate the corresponding mock light curves by following the same procedure mentioned above. Again, the real sampling patterns and measurement noise are taken into consideration. We repeat this process 400 times (i.e., for each source, 400 mock light curves with the same cadence and measurement noise are generated).

The mock ensemble structure functions for the 1900 Å, 2400 Å, 3180 Å and 4150 Å cases are shown in Figures 5–8, respectively. Just like the observed ensemble structure functions, our mock ensemble structure functions depend weakly on $M_{\rm BH}$ (see each of the row panels in Figures 5–8) but highly anti-correlate with L_{3000} and $\lambda_{\rm rest}$ (see Figure 9 and the column panels in Figures 5–8). That is, without fine-tuning of the model parameters, our mock ensemble structure functions are broadly consistent with the observed ones.

To quantitatively assess our modeling results, we calculate the following statistic for each bin,

$$\hat{S} = \text{Median} \left(\frac{(\overline{\log_{10} \text{SF}(\Delta t)} - \log_{10} \text{SF}_{\text{obs}}(\Delta t))^2}{\sigma_{\text{SF}}^2} \right), \quad (3)$$

where $\overline{\log_{10} \mathrm{SF}(\Delta t)}$, σ_{SF} , and $\log_{10} \mathrm{SF}_{\mathrm{obs}}(\Delta t)$ are the mean of the decimal logarithm of the 400 model ensemble structure functions, its 1σ uncertainty (i.e., the standard deviation of the 400 model ensemble structure functions), and the decimal logarithm of the observed ensemble structure function, respectively. Note that only $\Delta t > 10$ days are considered, as

Table 1
The Statistical Parameters for the Two Models

Statistical	The	The	The	The
Parameters ^a	1900 Å Case	2400 Å Case	3180 Å Case	4150 Å Case
p_0 p_1	$5.62 \times 10^{-2} $ 2.83×10^{-7}	$6.77 \times 10^{-2} $ 1.03×10^{-4}	$1.94 \times 10^{-3} $ 2.70×10^{-2}	$1.63 \times 10^{-2} \\ 8.84 \times 10^{-3}$
$\ln L_0$ $\ln L_1$	-0.56 -12.23	-0.37 -6.29	-3.52 -1.32	-1.60 -2.23
AIC ₀	9.12	8.74	15.04	11.21
AIC ₁	32.46	20.59	10.65	12.47

Note

measurement noise dominates over quasar variability on shorter time intervals. Our definition of \hat{S} is similar to the traditional reduced χ^2 statistic, but is more robust against outliers. The modeling statistic for each case is then defined as

$$\hat{S}_{\text{tot}} = \sum_{i=1}^{N} \hat{S}_i,\tag{4}$$

where N is the number of bins in each case. The expected distribution of the statistic \hat{S}_{tot} is unknown because the adjacent SF estimates are correlated and the light curves have irregular gaps. However, we can infer the distribution by using simulations. That is, we use Equations (3) and (4) to obtain the mock \hat{S}_{tot} (hereafter $\hat{S}_{\text{tot,mc}}$) for each of the 400 mock ensemble structure functions (i.e., replacing SF_{obs} in Equation (3) with a mock ensemble structure function). Then, for each case, we find that the histogram of $\hat{S}_{\text{tot,mc}}$ can be described by a Gamma distribution. Hence, we fit each distribution of $\hat{S}_{\text{tot,mc}}$ with a Gamma distribution. We use the Kolmogorov–Smirnov test to justify our best-fitting distribution and confirm that the null hypothesis (i.e., the best-fitting Gamma distribution is consistent with the observed one) cannot be rejected.

For each case, we use the best-fitting Gamma distribution to calculate the following statistical parameters, i.e., the probability of $\hat{S}_{\text{tot,mc}} > \hat{S}_{\text{tot}}$ (hereafter p_0), the natural logarithm likelihood of $\hat{S}_{\text{tot,mc}} = \hat{S}_{\text{tot}}$ (hereafter $\ln L_0$), and the Akaike information criterion (AIC; Akaike 1974). The AIC is defined as follows:

$$AIC = 2f - 2\ln L_0, \tag{5}$$

where f = 4 is the number of model parameters. The values of the three statistical parameters are listed in Table 1.

For the 1900 and 2400 Å cases, the corresponding p_0 values are much larger than 0.01; that is, at a significance level of 0.01, we cannot reject the null hypothesis that the differences between our mock ensemble structure functions and the observed ones are due to statistical fluctuations. For the 3180 and 4150 Å cases, their p_0 values are close than to even smaller than 0.01; we argue that this deviation is because the galaxy

²⁰ We choose this case because the light curves are mostly from r-band observations whose measurement uncertainties are the smallest among the five filters.

^a Subscripts 0 and 1 refer to models I and II, respectively.

 $[\]overline{^{21}}$ For the 4150 Å case, only data points with $\Delta t > 20$ days are considered. We use a larger Δt cut because the intrinsic variability of this case is the smallest among the four cases.

²² This argument is also valid if we adopt the traditional χ^2 statistic. For a detailed discussion of this point, refer to Emmanoulopoulos et al. (2010) and references therein.

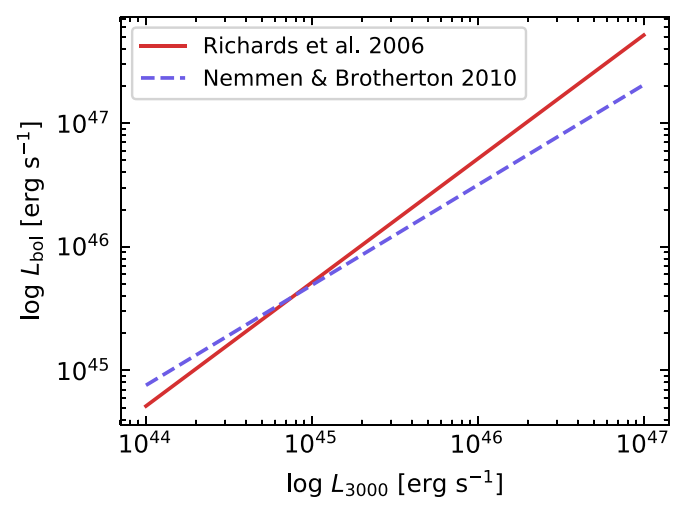


Figure 4. Constant and the luminosity-dependent bolometric corrections. For luminous sources, the bolometric correction of Nemmen & Brotherton (2010) is smaller than the constant one.

stellar light dilutes the $\lambda_{\rm rest} = 3180\,\text{Å}$ and $\lambda_{\rm rest} = 4150\,\text{Å}$ emission variability. Indeed, the differences between the mock and observed ensemble structure functions are prominent only in those $L_{\rm bol} < 10^{46}\,\rm erg\,\,s^{-1}$ bins (see Figure 8). All in all, we conclude that the CHAR model can satisfactorily reproduce the dependence of quasar UV/optical variability upon $M_{\rm BH}$, $L_{\rm bol}$, and $\lambda_{\rm rest}$, without any fine-tuning.

3.2. Model II: A Luminosity-dependent Bolometric Correction

Our model light curves are sensitive to $M_{\rm BH}$ and $L_{\rm bol}$ (or \dot{M}). There is growing evidence that the current virial black hole mass estimators (using either H β or Mg II) suffer from significant systematic biases (e.g., Grier et al. 2017; Du et al. 2018; Fonseca Alvarez et al. 2020). The accuracy of $M_{\rm BH}$ estimation might be greatly improved in ongoing or future RM campaigns (e.g., SDSS-RM; see Shen et al. 2016; Grier et al. 2017). Meanwhile, some previous works also suggested that the bolometric corrections of the rest frame 3000 or 5100 Å are not constant but depend on $L_{\rm bol}$ (e.g., Nemmen & Brotherton 2010; Netzer 2019). For instance, Nemmen & Brotherton (2010) calculated the spectral energy distributions of thin accretion disks with various $M_{\rm BH}$, $L_{\rm bol}$, and inclination angles and found the following alternative bolometric correction:

$$\log L_{\text{bol}} = C_1 + C_2 \log L_{3000},\tag{6}$$

where $C_1 = 9.24$ and $C_2 = 0.81$. An almost identical relation was obtained by Netzer (2019). We also try to use this bolometric correction to estimate $L_{\rm bol}$ (or \dot{M}) and repeat the modeling procedures in Section 3.1 to obtain the new mock ensemble structure functions.

Compared with model I, the mock ensemble structure functions of model II for high-luminosity bins have larger variability amplitudes. This is simply because, for high-luminosity bins, the bolometric correction of Nemmen & Brotherton (2010) is smaller than (see Figure 4) that of Richards et al. (2006).

We can also calculate the following three statistical parameters, i.e., the probability of $\hat{S}_{\text{tot,mc}} > \hat{S}_{\text{tot}}$ (hereafter p_1), the natural logarithm likelihood of $\hat{S}_{\text{tot,mc}} = \hat{S}_{\text{tot}}$ (hereafter $\ln L_1$), and the AIC (hereafter AIC₁) for model II. Their values are also listed in Table 1. For all but one case, we can reject the

null hypothesis that the mock ensemble structure functions are consistent with the observed ones at a significance level of 0.01; for the 3180 Å case, its p_0 value is slightly larger than 0.01. The total AIC of model II is also larger than that of model I with a difference of 32.06. Hence, we can conclude that model I with the constant bolometric correction of Richards et al. (2006) is favored over model II with the luminosity-dependent bolometric correction of Nemmen & Brotherton (2010). Our result is consistent with some independent works (e.g., Runnoe et al. 2012; Duras et al. 2020) that also found that the bolometric correction for L_{3000} is constant over seven luminosity decades.

4. Discussion

As demonstrated in previous sections and Sun et al. (2020), our CHAR model has the potential to satisfactorily explain many aspects of quasar UV/optical variability, including its dependence upon quasar physical properties. This is because the ratio of the observed to thermal timescales ($\tau_{\rm TH}$) almost determines the variability behavior (i.e., the variability behavior is nearly $\tau_{\rm TH}$ -scale-invariant; see Section 2.2 of Sun et al. 2020), and the thermal timescale scales as $\alpha^{-1}\dot{M}^{0.5}\lambda_{\rm rest}^2$. If we increase $L_{\rm bol}$, the thermal timescale also increases, as $\dot{M} = L_{\rm bol}/(\eta c^2)$ and the variability amplitude decreases. Hence, our CHAR model provides a natural explanation of the dependence of quasar UV/optical variability upon $L_{\rm bol}$, and our modeling results are able to distinguish between the constant and luminosity-dependent bolometric corrections.

Just like the luminosity-dependent bolometric corrections of Nemmen & Brotherton (2010) and Netzer (2019), our CHAR model is largely based on the classical thin-disk model (SSD; Shakura & Sunyaev 1973). Thus, why do our CHAR modeling results favor a constant bolometric correction? We speculate that this is because, as pointed out by Netzer (2019), the unknown parameters, e.g., SMBH spin and sightline, can introduce significant uncertainties to the bolometric corrections; hence, the performance of the SSD-based bolometric corrections is worse than that of the simple constant correction.

According to our CHAR model, for fixed frequency ranges (or fixed time samplings), the shapes of the power spectral densities (PSDs) of low-luminosity sources are flatter than their high-luminosity counterparts. The physical reasons are as follows. First, the shape of our model PSD is almost the same if the frequency is expressed in units of τ_{TH} (see Section 2.2 and Figure 15 of Sun et al. 2020). On timescales much less than au_{TH} , the disk temperature cannot respond to the fluctuations of the heating rate and the variations of the blackbody disk emission are suppressed, i.e., the PSD declines steeply at high frequencies (i.e., small $\Delta t/\tau_{\rm TH}$). On long timescales (comparable with or larger than τ_{TH}), the disk temperature can vary in response to the fluctuations of the heating rate and the variations of the disk emission are preserved. Second, the thermal timescale τ_{TH} scales as $\dot{M}^{0.5}\lambda^2$. For fixed observational timescales (Δt), high-luminosity sources have small $\Delta t/\tau_{\rm TH}$ and their light curves can only probe the steep parts of the PSDs. On the other hand, low-luminosity sources have large $\Delta t/\tau_{\rm TH}$ and their light curves can probe the flat parts of the PSDs. Such a dependence is found for the SDSS S82 quasars by Caplar et al. (2017). Very recently, Burke et al. (2020) used the optical light curve of NGC 4395 from the Transiting Exoplanet Survey Satellite to probe its hours-to-weeks optical variability and found that the PSD is consistent with that of the

Structure function for $\lambda_{eff} = 1908$ Å

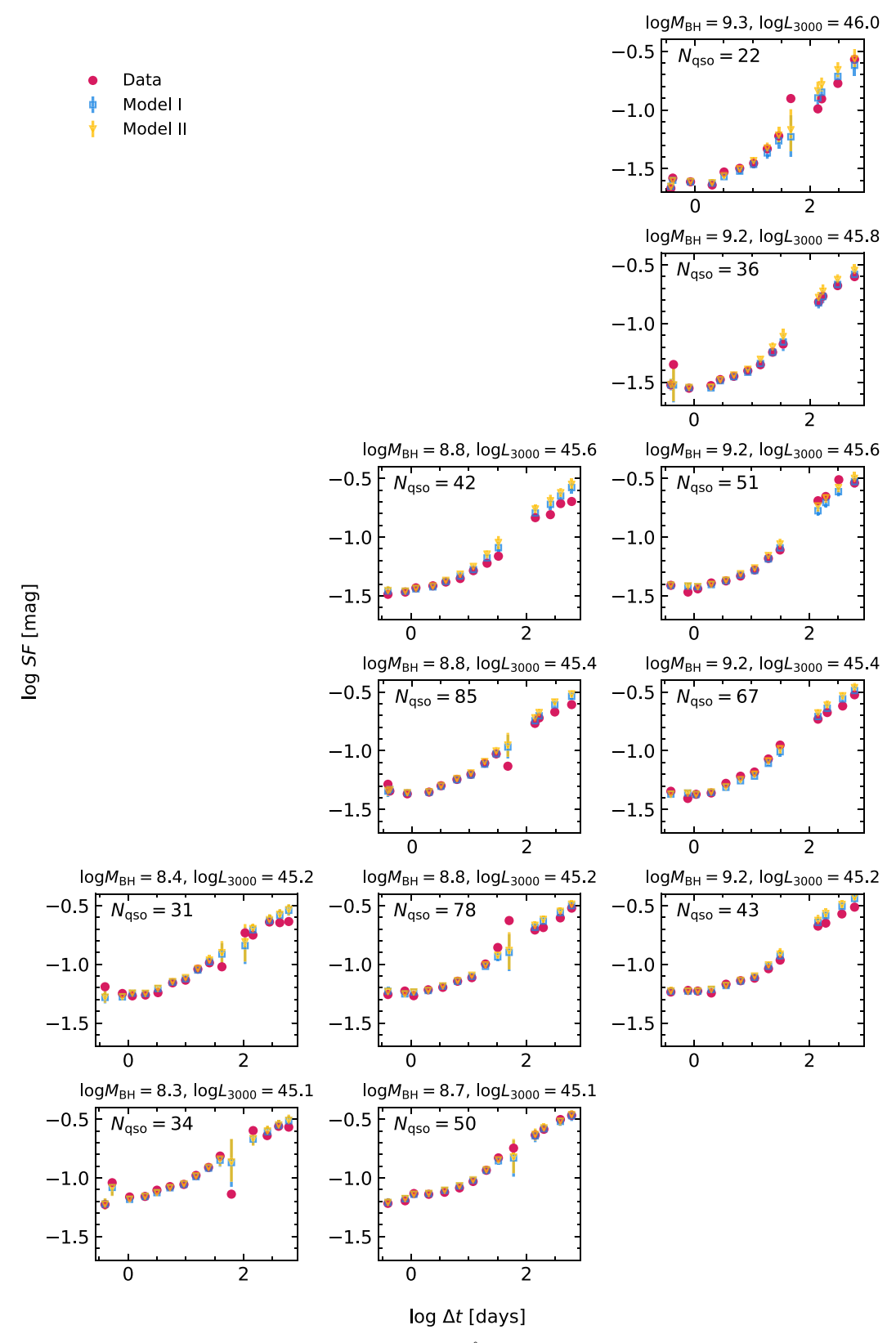


Figure 5. Ensemble structure functions for different $[M_{\rm BH}, L_{3000}]$ bins of the 1900 Å case. Panels in each column (row) share the same $M_{\rm BH}$ (L_{3000}). The data is obtained from the SDSS S82 quasar light curves. The only difference in models I and II is about the bolometric corrections used to convert L_{3000} into $L_{\rm bol}$. In model I, we use a constant bolometric correction of 5.15; in model II, a luminosity-dependent bolometric correction of Nemmen & Brotherton (2010) is adopted. Note that a few structure function data points show strong fluctuations which is simply caused by sampling issues. The error bars indicate the standard deviations of the 400 model ensemble structure functions of Model I and II. The time interval Δt is in rest frame. The gap around the rest frame 100 days is caused by the lack of timescale coverage of SDSS S82 quasar light curves.

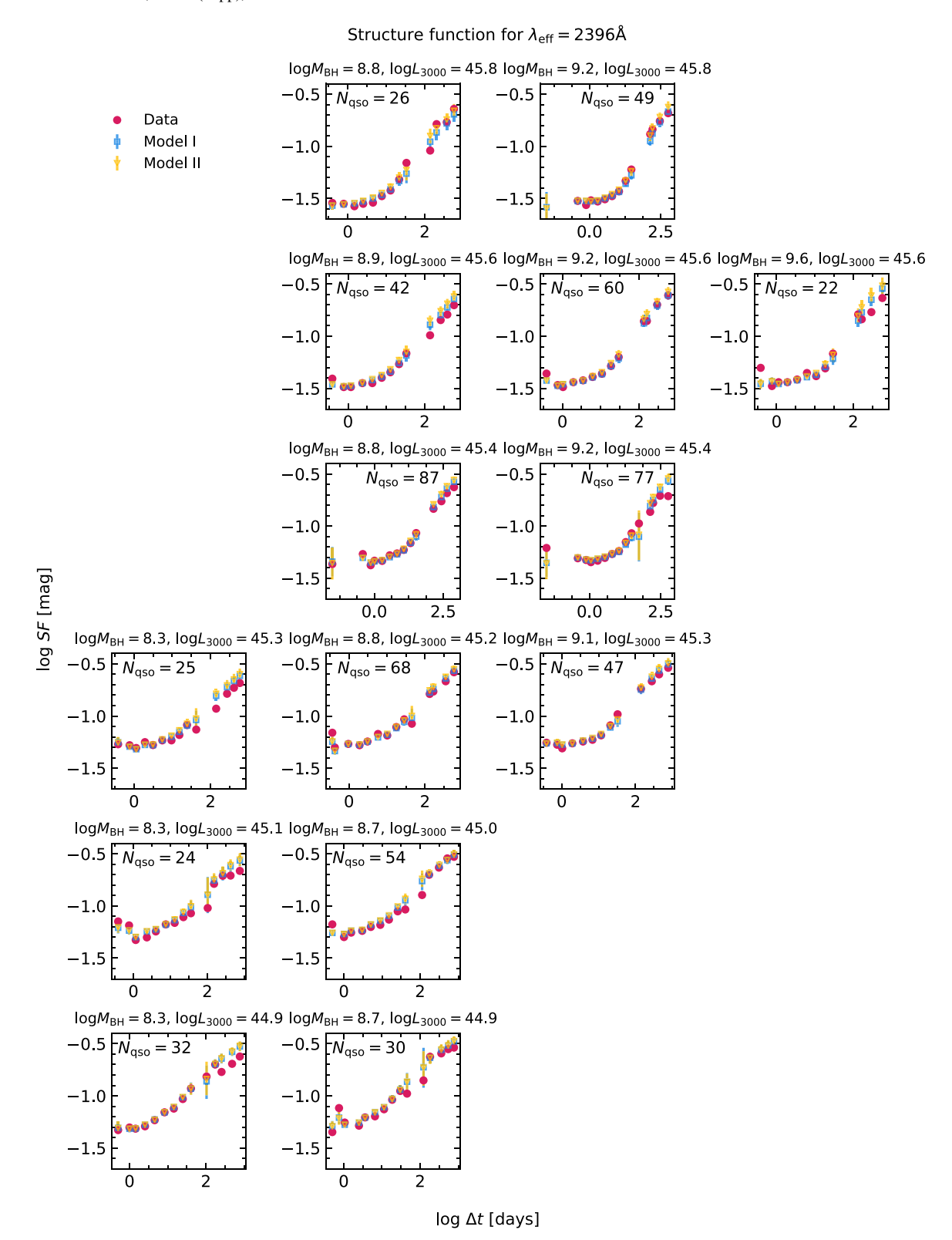


Figure 6. Ensemble structure functions for different [$M_{\rm BH}$, L_{3000}] bins of the 2400 Å case. Panels in each column (row) share the same $M_{\rm BH}$ (L_{3000}).

CAR (1) model. This result seems to be incompatible with the Kepler observations (Mushotzky et al. 2011). Our CHAR model provides a natural explanation for this apparent inconsistency. The bolometric luminosity of NGC 4395 is fainter than that of the best-studied Kepler AGN Zw 229-15 by a factor of 10^3 , i.e., (for fixed α and $\lambda_{\rm rest}$) the thermal timescale

of the former is $10^{1.5} \sim 30$ times shorter than that of the latter (since the thermal timescale $\propto \dot{M}^{0.5}$). As shown by Kelly et al. (2014), the PSD of Zw 229-15 approaches the f^{-2} relation on timescales $\geqslant 10$ days (and our CHAR model indeed reproduces this behavior; see Figure 18 of Sun et al. 2020). Therefore, according to our CHAR model, on timescales $\geqslant 10/30 = 1/3$

Structure function for $\lambda_{eff} = 3177$ Å

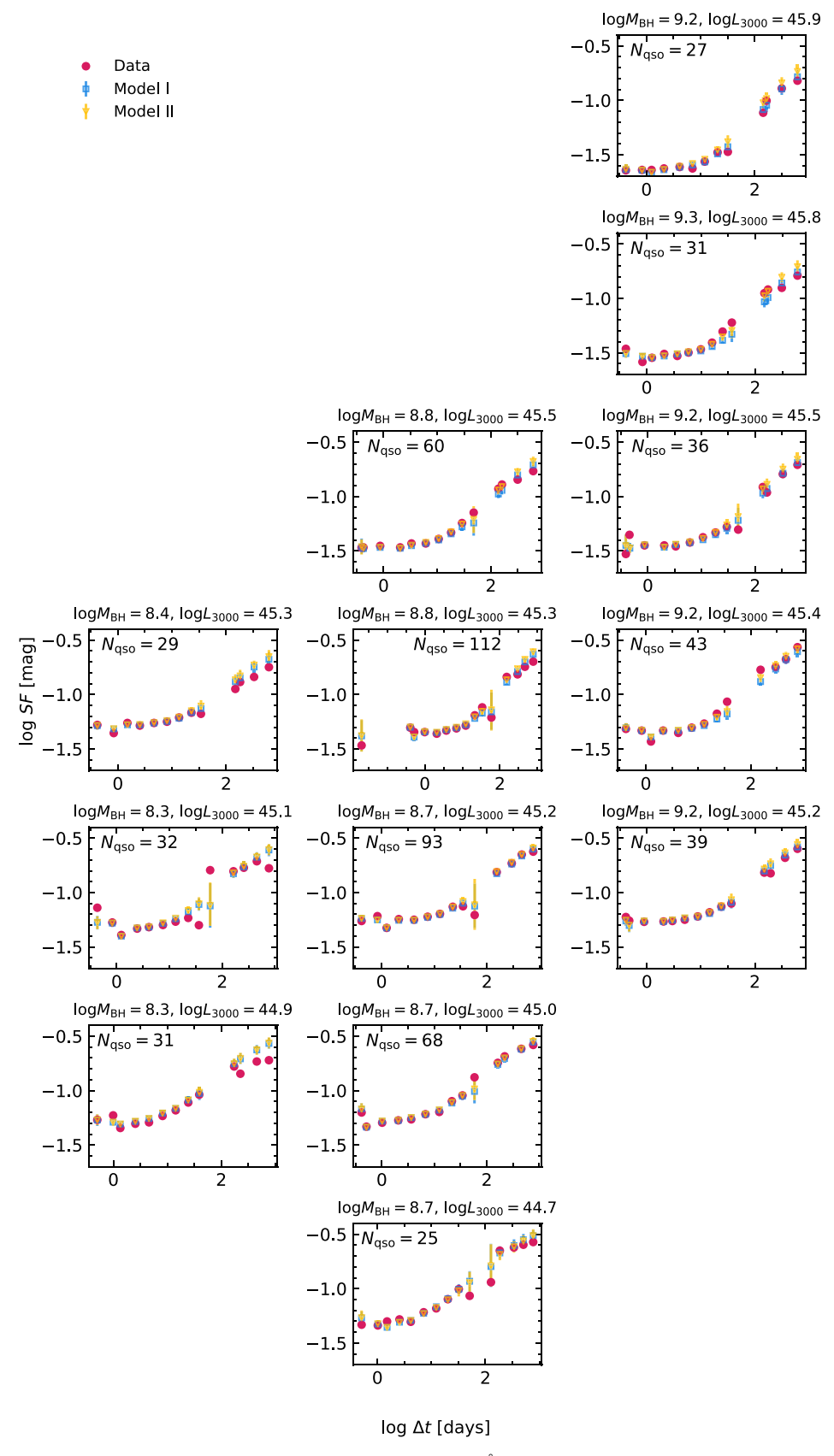


Figure 7. Ensemble structure functions for different $[M_{\rm BH}, L_{3000}]$ bins of the 3180 Å case. Panels in each column (row) share the same $M_{\rm BH}$ (L_{3000}).

Structure function for $\lambda_{\text{eff}} = 4152\text{\AA}$

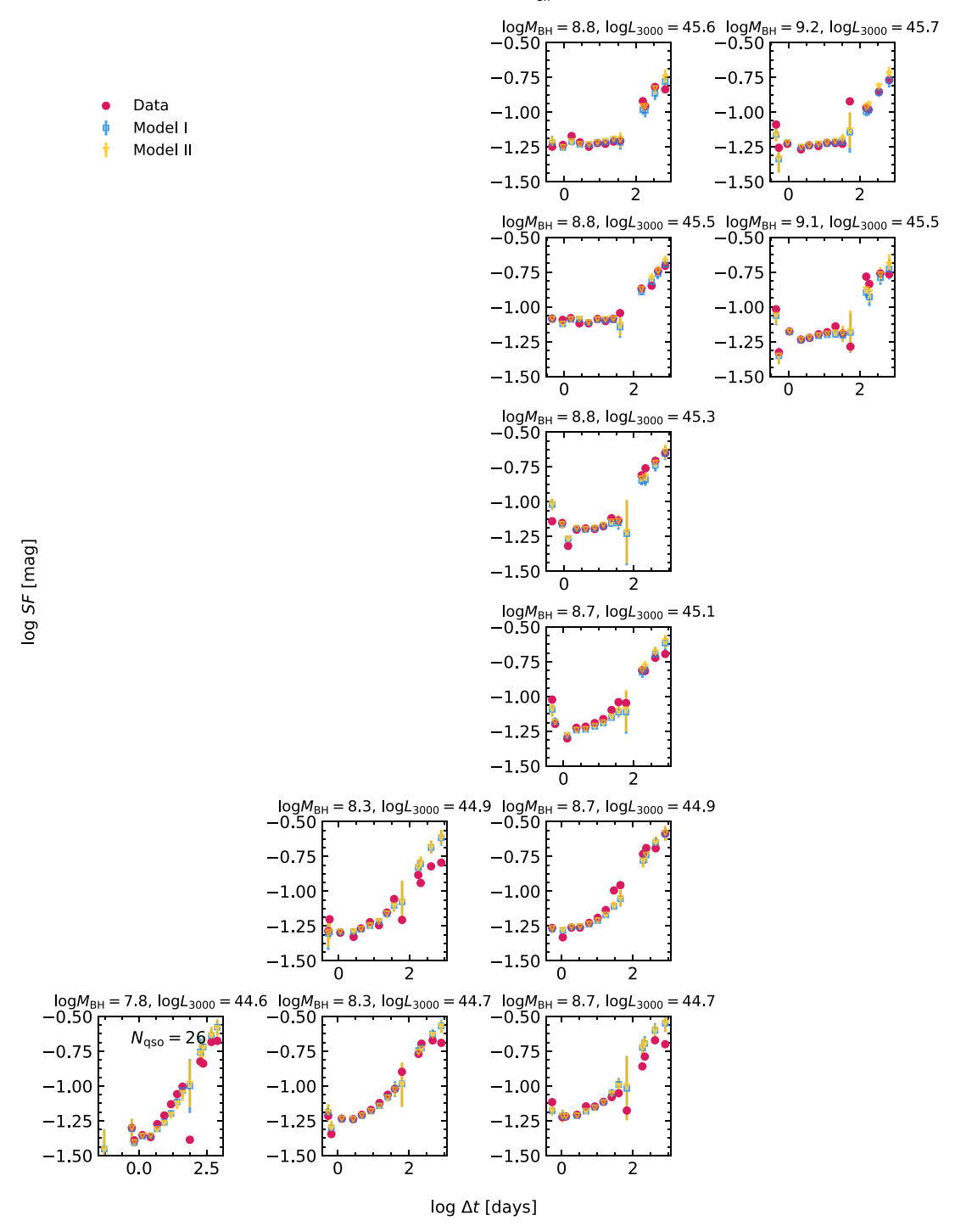


Figure 8. Ensemble structure functions for different [$M_{\rm BH}$, L_{3000}] bins of the 4150 Å case. Panels in each column (row) share the same $M_{\rm BH}$ (L_{3000}).

days (i.e., $f \le 3$ day⁻¹), the PSD of NGC 4395 is also expected to follow the f^{-2} relation.

For fixed $L_{\rm bol}$ and $\lambda_{\rm rest}$, our CHAR model predicts that quasar UV/optical variability amplitude increases slightly with $M_{\rm BH}$ (see Figure 13 of Sun et al. 2020); this prediction is also consistent with SDSS S82 observations (see the row panels in Figures 5–8). For fixed $M_{\rm BH}$ and $L_{\rm bol}$, the thermal timescale correlates with $\lambda_{\rm rest}$; therefore, the UV continuum is more variable than the optical one (see Figure 9).

When modeling the ensemble structure functions, α is fixed for all sources. If α is allowed to decrease with increasing $L_{\rm bol}$, we can also reproduce the observed ensemble structure functions with the luminosity-dependent bolometric correction (see Equation (6)). However, as the constant bolometric correction for L_{3000} is also favored in other independent works (e.g., Runnoe et al. 2012; Duras et al. 2020), our results indicate that the assumption of a constant α (i.e., α should depend at most weakly upon $M_{\rm BH}$ and $L_{\rm bol}$) is probably reasonable. This

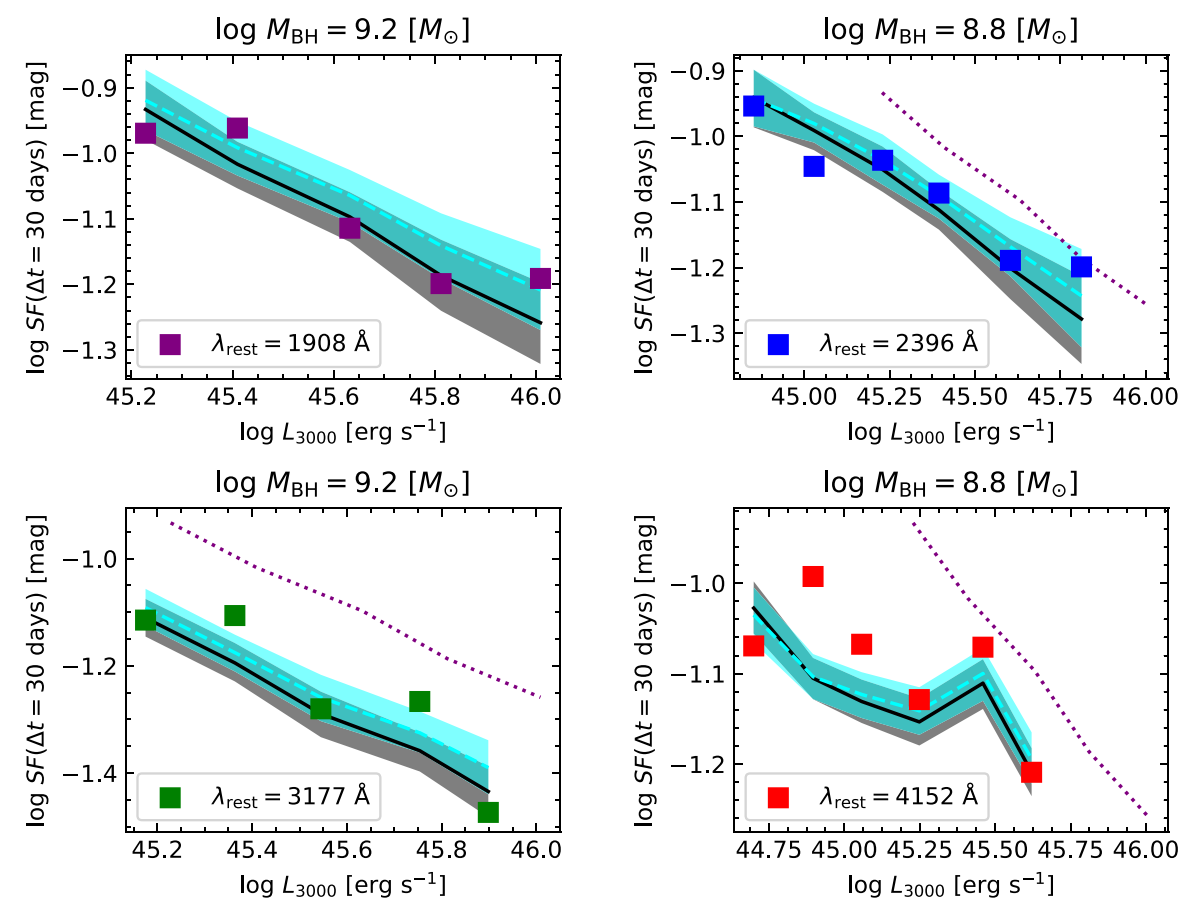


Figure 9. The ensemble structure functions at $\Delta t = 30$ days as a function of L_{3000} for the four wavelength cases. The purple, blue, green, and red squares represent the 1900 Å, 2400 Å, 3180 Å, and 4150 Å cases, respectively. The black solid (cyan dashed) curves and shaded regions correspond to the mean and 1σ uncertainties of the model I (II) results. Note that the model I ensemble structure function for the 1900 Å case (i.e., the purple dotted curve) is shown in every panel for the purpose of comparison. The complete figure set (three images) is available in the online journal and contains the $\Delta t = 30$, 100, and 300 days images. (The complete figure set (3 images) is available.)

conclusion is further supported by the similar α values found in the accretion disks around stellar black holes (whose $M_{\rm BH}$ and $L_{\rm bol}$ are several orders of magnitude smaller than AGNs) in their outburst phases (King et al. 2007). Note that, for fixed $L_{\rm bol}$, $\dot{M} \propto \eta^{-1}$ and η correlates with dimensionless SMBH spin parameter (a_* , which takes values from -1 to 1). In previous sections, we assume $\eta=0.1$, which corresponds to a moderate positive a_* . If the SDSS S82 SMBHs spin faster and have larger η , the inferred \dot{M} is smaller and so is the required α . Indeed, current X-ray spectroscopic observations (for a recent review, see Reynolds 2019) seem to find a large fraction of SMBHs with $a_*>0.9$ (but see Laor 2019).

There are still some small residuals between the two models and the observed ensemble structure functions. We test the possible correlations between the small residuals and quasar physical properties (i.e., $M_{\rm BH}$ and L_{3000}) and find that the correlations are statistically insignificant (i.e., the corresponding p_0 values are much greater than 0.01). We speculate that the small residuals are driven by the significant uncertainties of $M_{\rm BH}$ (for instance, while the $M_{\rm BH}$ estimators depend upon orientation, the variability amplitude should be insensitive to orientation; see, e.g., Sun et al. 2018b) and \dot{M} . It is also possible that quasar UV/optical variability might also

depend (weakly) upon other additional factors, e.g., X-ray loudness (Kang et al. 2018) or magnetic field (Cai et al. 2019).

5. Summary and Future Work

5.1. Summary

We use our CHAR model to reproduce SDSS S82 quasar UV/optical variability. Our main results are summarized as follows:

- 1. The CHAR model can broadly reproduce the observed ensemble structure functions of SDSS S82 quasars with various $M_{\rm BH}$, $L_{\rm bol}$, and $\lambda_{\rm rest}$ without fine-tuning the model parameters.
- Our variability modeling results are in favor of a constant bolometric correction for the 3000 Å continuum luminosity.
- 3. The dimensionless viscosity parameter α should depend only weakly on $M_{\rm BH}$ and $L_{\rm bol}$.
- Based on our physical modeling results, we present a recipe to simulate AGN UV/optical light curves.

Compared with empirical model-fitting results, our results demonstrate a new way to directly infer quasar properties (e.g.,

the bolometric correction, the dimensionless viscosity dimensionless parameter) by physically modeling their multiwavelength light curves.

5.2. Future Work

Future time-domain surveys like the Legacy Survey of Space and Time (LSST) will provide well-sampled (with a cadence of $\sim\!\!3$ days) light curves for $\gtrsim\!\!10^4$ AGNs (Brandt et al. 2018; Scolnic et al. 2018). Combining the LSST light curves with archival observations or the sparse but deep multiband observations of the Chinese Space Station Telescope (Zhan 2011; Cao et al. 2018), the light curves can cover an observed-frame timescale of over 30 yr. In the future, we will use the CHAR model to simulate mock LSST AGN light curves 23 and explore AGN UV/optical variability on very long timescales (e.g., MacLeod et al. 2012; Caplar et al. 2020).

M.Y.S. acknowledges support from the National Natural Science Foundation of China (NSFC-11973002, NSFC-11873045). Y.Q.X. and J.X.W. acknowledge support from the National Natural Science Foundation of China (NSFC-11890693, 11421303, and 12033006), the CAS Frontier Science Key Research Program (QYZDJ-SSW-SLH006), and the K.C. Wong Education Foundation. W.N.B. acknowledges support from NSF grant AST-1516784 and NASA ADAP grant 80NSSC18K0878. T.L. acknowledges support from the National Natural Science Foundation of China (NSFC-11822304).

Software: Matplotlib (Hunter 2007), Numpy & Scipy (Van Der Walt et al. 2011), pyLCSIM (Campana 2017).

ORCID iDs

Mouyuan Sun https://orcid.org/0000-0002-0771-2153
Yongquan Xue https://orcid.org/0000-0002-1935-8104
Hengxiao Guo https://orcid.org/0000-0001-8416-7059
Junxian Wang https://orcid.org/0000-0002-4419-6434
W. N. Brandt https://orcid.org/0000-0002-0167-2453
Jonathan R. Trump https://orcid.org/0000-0002-1410-0470
Zhicheng He https://orcid.org/0000-0003-3667-1060
Tong Liu https://orcid.org/0000-0001-8678-6291
Jianfeng Wu https://orcid.org/0000-0001-7349-4695

References

```
Akaike, H. 1974, ITAC, 19, 716
Blandford, R. D., & McKee, C. F. 1982, ApJ, 255, 419
Brandt, W. N., Ni, Q., Yang, G., et al. 2018, arXiv:1811.06542
Burke, C. J., Shen, Y., Chen, Y.-C., et al. 2020, ApJ, 899, 136
```

```
Butler, N. R., & Bloom, J. S. 2011, AJ, 141, 93
Cai, Z., Sun, Y., Wang, J., et al. 2019, SCPMA, 62, 69511
Campana, R. 2017, pyLCSIM: X-ray Lightcurves Simulator v0.4.0,
   Astrophysics Source Code Library, ascl:1708.016
Cao, Y., Gong, Y., Meng, X.-M., et al. 2018, MNRAS, 480, 2178
Caplar, N., Lilly, S. J., & Trakhtenbrot, B. 2017, ApJ, 834, 111
Caplar, N., Pena, T., Johnson, S. D., et al. 2020, ApJL, 889, L29
Coatman, L., Hewett, P. C., Banerji, M., et al. 2017, MNRAS, 465, 2120
Collin-Souffrin, S. 1991, A&A, 249, 344
Denney, K. D. 2012, ApJ, 759, 44
Du, P., Zhang, Z.-X., Wang, K., et al. 2018, ApJ, 856, 6
Duras, F., Bongiorno, A., Ricci, F., et al. 2020, A&A, 636, A73
Emmanoulopoulos, D., McHardy, I. M., & Uttley, P. 2010, MNRAS,
   404, 931
Fonseca Alvarez, G., Trump, J. R., Homayouni, Y., et al. 2020, ApJ, 899, 73
Fukugita, M., Ichikawa, T., Gunn, J. E., et al. 1996, AJ, 111, 1748
Grier, C. J., Trump, J. R., Shen, Y., et al. 2017, ApJ, 851, 21
Gunn, J. E., Siegmund, W. A., Mannery, E. J., et al. 2006, AJ, 131, 2332
Guo, H., Wang, J., Cai, Z., et al. 2017, ApJ, 847, 132
He, Z., Wang, T., Liu, G., et al. 2019, NatAs, 3, 265
Hunter, J. D. 2007, CSE, 9, 90
Kang, W.-. y., Wang, J.-X., Cai, Z.-Y., et al. 2018, ApJ, 868, 58
Kelly, B. C., Bechtold, J., & Siemiginowska, A. 2009, ApJ, 698, 895
Kelly, B. C., Becker, A. C., Sobolewska, M., Siemiginowska, A., & Uttley, P.
   2014. ApJ. 788. 33
King, A. R., Pringle, J. E., & Livio, M. 2007, MNRAS, 376, 1740
Krolik, J. H., Horne, K., Kallman, T. R., et al. 1991, ApJ, 371, 541
Laor, A. 2019, NatAs, 3, 374
Lawrence, A. 2018, NatAs, 2, 102
Li, J., Sun, M., Wang, T., et al. 2019, MNRAS, 487, 4592
MacLeod, C. L., Ivezić, Ž., Kochanek, C. S., et al. 2010, ApJ, 721, 1014
MacLeod, C. L., Ivezić, Ž., Sesar, B., et al. 2012, ApJ, 753, 106
Marziani, P., del Olmo, A., Martínez-Carballo, M. A., et al. 2019, A&A,
Mushotzky, R. F., Edelson, R., Baumgartner, W., & Gandhi, P. 2011, ApJL,
   743, L12
Nemmen, R. S., & Brotherton, M. S. 2010, MNRAS, 408, 1598
Netzer, H. 2019, MNRAS, 488, 5185
Reynolds, C. S. 2019, NatAs, 3, 41
Richards, G. T., Kruczek, N. E., Gallagher, S. C., et al. 2011, AJ, 141, 167
Richards, G. T., Lacy, M., Storrie-Lombardi, L. J., et al. 2006, ApJS, 166, 470
Runnoe, J. C., Brotherton, M. S., & Shang, Z. 2012, MNRAS, 422, 478
Scolnic, D. M., Lochner, M., Gris, P., et al. 2018, arXiv:1812.00516
Sesar, B., Ivezić, Ž., Lupton, R. H., et al. 2007, AJ, 134, 2236
Shakura, N. I., & Sunyaev, R. A. 1973, A&A, 24, 337
Shen, Y. 2013, BASI, 41, 61
Shen, Y., Horne, K., Grier, C. J., et al. 2016, ApJ, 818, 30
Shen, Y., Richards, G. T., Strauss, M. A., et al. 2011, ApJS, 194, 45
Ivezić, Ž., Smith, J. A., Miknaitis, G., et al. 2007, AJ, 134, 973
Smith, K. L., Mushotzky, R. F., Boyd, P. T., et al. 2018, ApJ, 857, 141
Sun, M., Trump, J. R., Shen, Y., et al. 2015, ApJ, 811, 42
Sun, M., Xue, Y., Brandt, W. N., et al. 2020, ApJ, 891, 178
Sun, M., Xue, Y., Richards, G. T., et al. 2018a, ApJ, 854, 128
Sun, M., Xue, Y., Wang, J., Cai, Z., & Guo, H. 2018b, ApJ, 866, 74
Van Der Walt, S., Colbert, S. C., & Varoquaux, G. 2011, CSE, 13, 22
Vanden Berk, D. E., Richards, G. T., Bauer, A., et al. 2001, AJ, 122, 549
Zhan, H. 2011, SSPMA, 41, 1441
Zuo, W., Wu, X.-B., Fan, X., et al. 2020, ApJ, 896, 40
```

 $[\]frac{23}{1}$ The authors are willing to share the simulated light curves upon request.